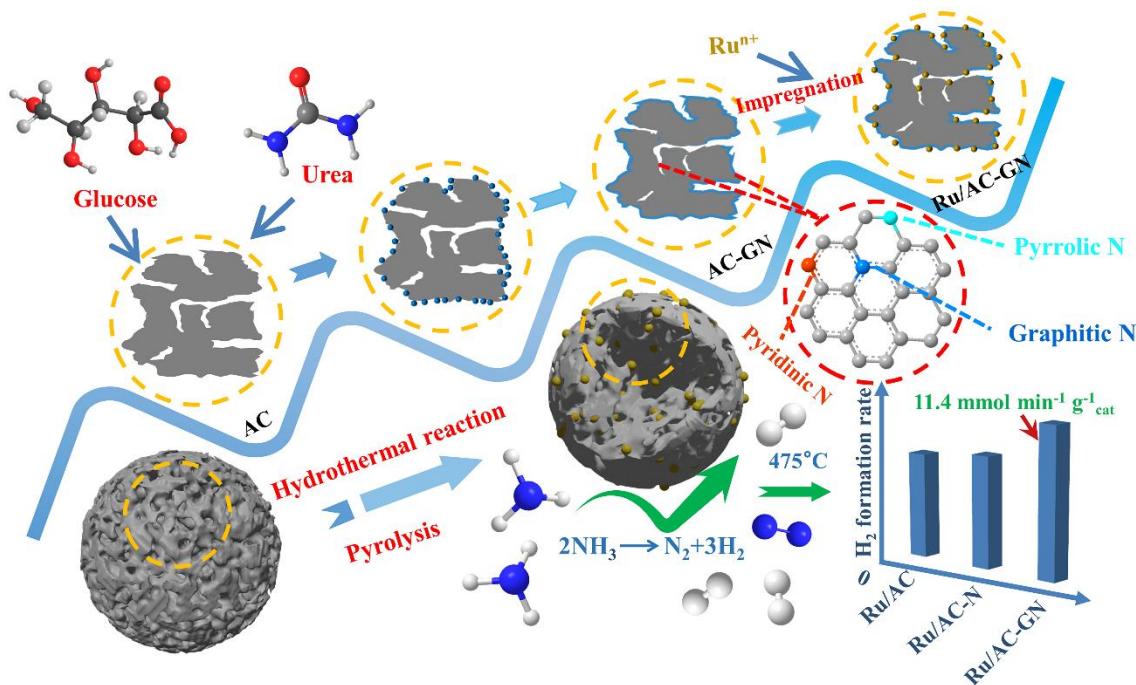# Enhanced Activity of Ru-based Catalysts for Ammonia Decomposition through Nitrogen Doping of Hierarchical Porous Carbon Carriers

Rui Wang,[a] Xiuxiu Chen,[a] Han Hao,[b] Bing Wang,[a] Hewei Yu,[a,*] Meng Wang,[c] Yongjun Xie,[d] Jianmei Wang,[a,*] and Hongyu Si [a,*]

Corresponding authors: yhw@qlu.edu.cn (H. YU), wangjm@sderi.cn (J. Wang), sihy@sderi.cn (H. Si).

GRAPHICAL ABSTRACT

Enhanced Activity of Ru-based Catalysts for Ammonia Decomposition through Nitrogen Doping of Hierarchical Porous Carbon Carriers

Rui Wang,[a] Xiuxiu Chen,[a] Han Hao,[b] Bing Wang,[a] Hewei Yu,[a,*] Meng Wang,[c] Yongjun Xie,[d] Jianmei Wang,[a,*] and Hongyu Si [a,*]

Activated carbon (AC) materials, renowned for their high specific surface area, excellent conductivity, and customizable functional groups, are widely employed as catalyst carriers. However, enhancing the activity of Ru-based catalysts supported on AC (Ru/AC) for ammonia decomposition remains a challenge. In this study, commercial AC was utilized as a substrate, with glucose and urea employed as modifiers. Specifically, the surface of the AC was modified *via* a hydrothermal pyrolysis method, resulting in the successful post-treatment *in situ* co-doping of nitrogen (AC-GN). Experimental results revealed that Ru/AC-GN exhibited a hydrogen production rate 46% higher than that of Ru/AC at 475 °C, indicating improved activity and stability. The characterization of AC-GN demonstrated that nitrogen doping primarily occurred on the external surface and macropores of the AC, increasing the nitrogen content in the carrier, particularly pyrrolic nitrogen content, while preserving the original structural and morphological integrity of the AC. The enhanced dispersion of Ru, combined with the improved electronic transmission capabilities and strengthened interactions between the metal and the modified carrier, were identified as pivotal factors contributing to the enhanced low-temperature efficacy of Ru/AC-GN. This paper presents a novel direction for the large-scale preparation of efficient catalysts for ammonia decomposition.

INTRODUCTION

Hydrogen is widely recognized as an efficient and clean energy source, offering potential solutions to environmental pollution and the energy crisis (Mehrpooya and Habibi 2020; Wan *et al.* 2021). However, its low volumetric density and challenges associated with its storage and transportation, particularly liquefaction, pose significant barriers to its widespread application (Abe *et al*. 2019; Luo *et al.* 2020). In recent years, ammonia has garnered considerable attention as an effective hydrogen carrier owing to its high hydrogen content of 17.7 wt% alongside its liquid state at room temperature (25 °C) and low pressure

(6 atm). Additionally, its CO_X-free decomposition process and the relative maturity of ammonia storage and transport technologies make it a highly promising medium for H_2 storage and transportation (Chang *et al.* 2021; Sun *et al.* 2022).

The decomposition of ammonia for hydrogen production is considered a promising pathway for transitioning to clean energy and developing a hydrogen economy, despite existing technical challenges, particularly in enhancing decomposition efficiency and reducing costs (Lee *et al.* 2021). A key strategy involves the development of highly active catalysts that can operate effectively at temperatures below 500 °C (Mukherjee *et al.* 2018). Commonly used active metals in ammonia decomposition catalysts include Ru, Ni, and Co. Among them, Ru-based catalysts are the most frequently utilized, owing to their exceptional activity at low temperatures (Cao *et al.* 2022; Nakamura *et al.* 2022). Notably, catalytic activity is greatly influenced by the dispersibility, morphology, and size of Ru nanoparticles (Yao *et al.* 2011). The B5-type surface of Ru contains high-activity sites, and nanoparticles approximately 2 nm in size are considered to provide an increased number of B5-type sites (Zheng *et al.* 2007; Su *et al.* 2024). Karim *et al.* (2009) have demonstrated that the catalytic activity of spherical Ru nanoparticles ranging from 1.8 to 3 nm in size was the highest. Furthermore, extensive research has revealed a close relationship between the efficiency of NH_3 decomposition and factors such as alkaline environments and electron transfer capabilities (Tan *et al.* 2012; Nagaoka *et al.* 2014), which can be modulated by employing different carriers.

Porous carbon-based materials, known for their expansive specific surface area, adaptable functional groups, and exceptional conductivity, are widely employed as catalyst carriers (Yin *et al.* 2004a). The primary focus of research has centered on activated carbon (AC) and carbon nanotubes (CNTs) (Chen *et al.* 2021). For instance, Yin *et al.* (2004b) synthesized K-Ru/CNTs at 450 °C with an NH_3 flow rate of 60000 $mLg_{cat}^{-1} h^{-1}$, achieving a decomposition efficiency of 97.3% and hydrogen formation rate 32.6 mmol $g_{cat}^{-1}min^{-1}$, which significantly outperformed the 9.6 mmol $g_{cat}^{-1}min^{-1}$ hydrogen formation rate of Ru/AC. This enhancement is attributed to the high degree of graphitization in CNTs, facilitating electron transfer between the carrier and metal. There is a notable increase in the H_2 production rate by doping nitrogen into CNT carriers, primarily owing to enhanced electron interactions between the carrier and the metal, as well as the increased anchoring sites provided by nitrogen, which improve Ru particle dispersion (Hien *et al.* 2015; Ren *et al.* 2017). However, research on modifying AC *via* nitrogen doping for ammonia decomposition remains relatively limited.

Biomass carbon materials are considered excellent carrier materials from both environmental and cost perspectives. However, current research indicates that heteroatoms such as S, Cl, and N on the surface of AC can inhibit ammonia decomposition owing to low graphitization levels, impeding effective electron transfer between the metal and the carrier (Yin *et al.* 2004b). While heteroatoms can be removed by introducing H_2 at high temperatures (Raróg-Pilecka *et al.* 2003), the presence of defects benefits Ru anchoring, thereby enhancing dispersion (Rodríguez-reinoso 1998). Nevertheless, oxygen-containing functional groups on the surface can diminish the activity of Ru owing to their electron-withdrawing effect (Rarogpilecka *et al.* 2005). Consequently, a suitable nitrogen doping method must be chosen to strike an optimal balance. In this context, a pioneering approach uniformly anchors micrometer-sized carbon spheres onto the surface and within the large pores of commercial AC using glucose *via* a hydrothermal method, revealing a new direction for post-treatment nitrogen doping (Liu *et al.* 2010).

To enhance the performance of the AC carrier, a nitrogen-doping method based on hydrothermal pyrolysis was employed. Concurrently, nitrogen-doped hydrothermal carbon was deposited on the surface of the AC, achieving the post-treatment *in situ* co-doping of nitrogen. This method aimed to preserve the original pore structure and degree of graphitization to the greatest possible extent, while the introduction of nitrogen provides additional sites for Ru loading. Consequently, the performance of AC as an ammonia decomposition catalyst carrier is substantially enhanced, thereby offering a novel approach for preparing high-activity Ru/AC catalysts.

EXPERIMENTAL

Materials

AC, derived from coconut shells, was procured from Shanghai Ron Chemical Technology Co., Ltd., with the item number R019806. Urea (> 99%), glucose ($C_6H_{12}O_6$ > 99%), nitric acid (65 to 69%), and ruthenium (31.3%) were sourced from commercial suppliers and employed without additional purification.
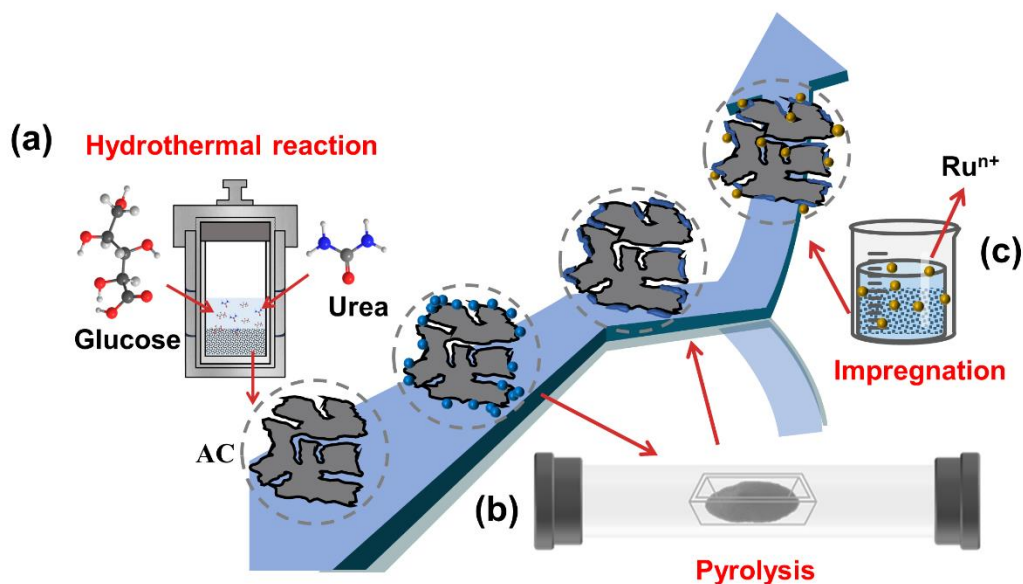

Fig. 1. Experimental process and detailed schematic diagram

Sample synthesis

The carrier was prepared by grinding a suitable amount of commercial AC to 20–40 mesh, referred to as AC henceforth in this paper. Subsequently, 5 g of AC was mixed with 200 mL of nitric acid for oxidative pretreatment, followed by multiple washes with deionized water and drying at 80 °C for 12 h, resulting in AC-O. Then, 1 g of AC-O and 1 g of urea were added to 20 mL of distilled water and stirred at room temperature for 30 min, followed by transferring the mixture to an autoclave. The autoclave was placed in an oven and maintained at 180 °C for 6 h. After cooling to room temperature, the sample was filtered and dried at 80 °C for 12 h (Figure 1a). The obtained sample was then placed in a tube furnace and calcined under a N_2 flow of 100 mL min^{-1}. The pyrolysis protocol involved heating the sample to 800 °C at a rate of 10 °C min^{-1}, holding the sample at this temperature for 1 h, and finally cooling it to room temperature. The resultant sample was

denoted as AC-N (Fig. 1b). Furthermore, AC-G and AC-GN were prepared using the same procedure, with the only difference being the substitution of 1 g of urea with 1 g of glucose and a combination of 1 g urea and 1 g glucose, respectively.

The catalysts were prepared using an equal volume impregnation method to achieve a 3 wt% Ru loading. Specifically, AC, AC-N, AC-G, and AC-G-N were ultrasonically mixed for 20 min, allowed to stand for 2 h, and then dried at 80 °C for 12 h to obtain catalysts with 3 wt% Ru loading, designated as Ru/AC, Ru/AC-N, Ru/AC-G, and Ru/AC-GN, respectively (Fig. 1c). The prepared catalysts were stored in sealed conditions.

Methods

Sample characterization

The samples underwent degassing under an N_2 atmosphere at 120 °C for 12 h. Specific surface area and pore volume were determined using an automatic surface area and porosity analyzer (BET, Beijing Jingwei Gaobo Company JW-BK132F, China). Surface composition analyses and semi-quantitative assessments of the samples were conducted using an X-ray photoelectron spectroscope (Thermo Scientific K-Alpha, USA). X-ray diffraction (XRD) scans were performed from 10° to 80° at a rate of 2° min^{-1} using a Rigaku D/max-2200pc instrument (Japan). Raman spectra were recorded with a Horiba LabRAM HR Evolution Raman spectrometer (Japan) using an excitation wavelength of 532 nm. Elemental composition was analyzed with an element analyzer (Elementar UNICUBE, Germany). Surface characteristics were explored *via* scanning electron microscopy (SEM, TESCAN MIRA LMS, Czech Republic), and the morphology and dispersion of catalysts, along with elemental types and contents, were investigated using a transmission electron microscope (JEOL JEM-F200). Crystal structure and elemental analyses were performed using a high-resolution transmission electron microscope combined with an energy-dispersive spectrometer. Thermogravimetric analysis (TG, Netzsch STA449F3, Germany) was performed under an N_2 atmosphere from 30 to 800 °C with a heating rate of 10 °C min^{-1}. H_2 temperature-programmed reduction (H_2-TPR) and N_2 temperature-programmed desorption (N_2-TPD) analyses were carried out using a temperature-programmed chemical adsorption instrument (Micromeritics Auto Chem II 2920, USA), with detailed procedures provided in the supplementary materials.

Catalyst Activity Tests

The catalytic activity of the various samples for ammonia decomposition was assessed at atmospheric pressure and 400 to 550 °C in a quartz tube reactor with an 8 mm inner diameter. Specifically, a 200 mg catalyst sample was activated under a 50% H_2 and 50% Ar mixed gas flow at 300 °C for 2 h. Following reduction, the system was purged with NH_3 for 30 min before initiating ammonia decomposition tests. Furthermore, the effluent gases (H_2, N_2, and NH_3) were analyzed using a gas chromatograph equipped with a thermal conductivity detector and a Porapak-Q column (Zhejiang Fuli GC-9720P, China). The corresponding methodological and calculation details are provided in Fig. S1.

Experimental and detection data were compiled using Excel 2021, while linear fitting and graph plotting were performed using Origin 2021. XPS peak deconvolution and fitting were conducted using Avantage 6.6. Phase analysis was performed using MDI Jade 6, while particle size statistics and lattice fringe measurements were performed using Nano Measurer 1.2 and Digital Micrograph 3.5.

RESULTS AND DISCUSSION

Structural Characteristics of Carriers and Catalysts

Figure 2 presents the adsorption–desorption isotherms and pore size distributions of the various samples. The specific surface area and pore structure of a carrier play a crucial role in determining the dispersion and size of active metal particles in supported catalysts (Ren *et al.* 2023; Du *et al.* 2024). As shown in Fig 2a, AC, AC-N, AC-G, and AC-GN exhibited similar N_2 adsorption–desorption isotherms, namely Type I isotherms with H1-type hysteresis loops (Calzaferri *et al.* 2023). The pore size distribution, depicted in Fig. 2b, indicates that the various modification techniques did not substantially alter the structure of AC, thereby preserving its hierarchical porous carbon architecture (micropore–mesopore–macropore), which facilitates the dispersion of active metals.
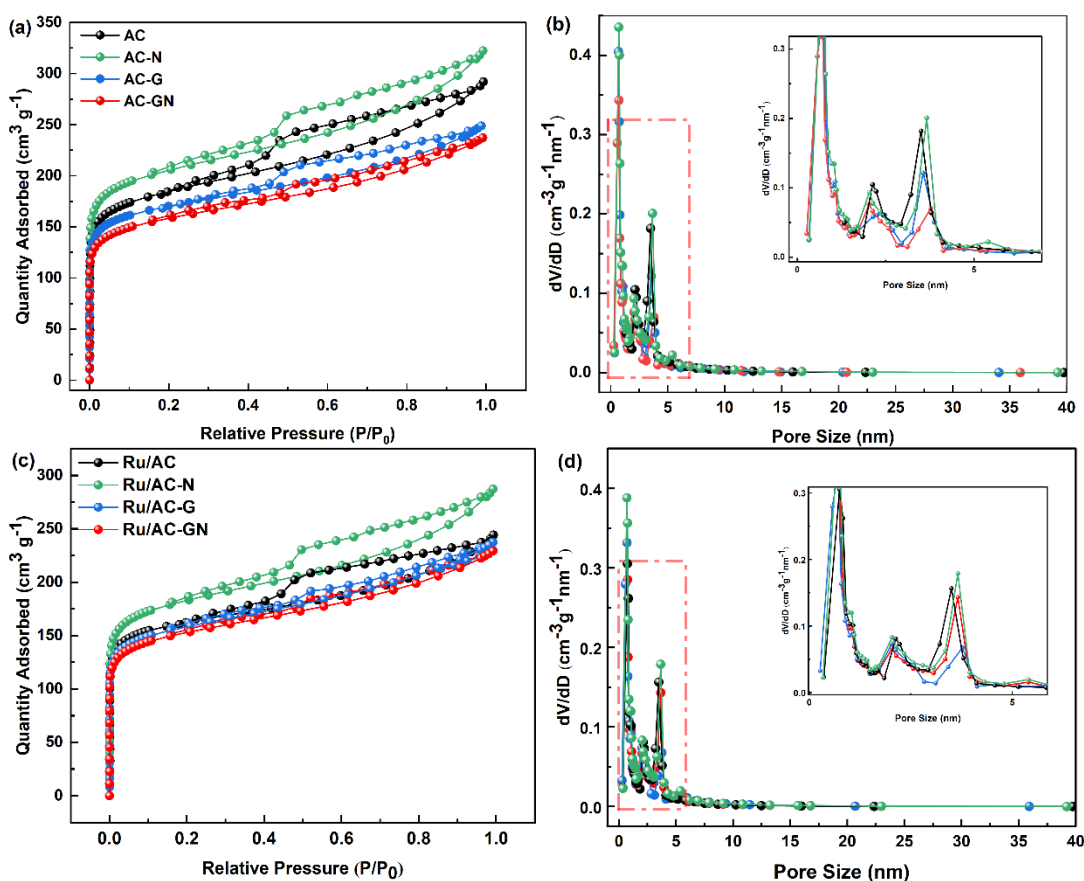

Fig. 2. N_2 sorption isotherms, (a) and (c), and pore size distribution curves, (b) and (d), of various supports and catalysts

Further analysis of specific surface area and pore structure data from Table 1 revealed that AC-N exhibited the highest specific surface area (750 m^2g^{-1}) and pore volume (0.49 cm^3g^{-1}), representing increases of 27% and 8%, respectively, compared to AC, while the average pore diameter decreased by 13%. This decrease can be attributed to the etching effect on the carbon structure caused by radicals generated during urea decomposition, leading to enhanced porosity (Stöhr *et al.* 1991). By contrast, AC-G showed a slight decrease in average pore diameter, specific surface area, and pore volume relative to AC. This decrease is attributed to the deposition of new carbon structures formed by glucose on

the surface and within the pores of AC. The specific surface area and pore volume of AC-GN were greater than those of AC-G, likely owing to urea decomposition. Given that the carbon microspheres formed during the hydrothermal reaction of glucose ranged between 50 to 200 nm in size (Liu *et al.* 2010), it is inferred that the carbon structures derived from glucose adhered to the external surface and large pores of AC. These findings suggest that the introduction of glucose did not significantly block the pores, thereby minimally impacting the micro and mesopores of AC. Consequently, this modification method preserved the original micro and mesoporous structures of the carrier alongside facilitating the formation of novel nitrogen-doped carbon structures on the outer surface and in the large pores. Figures 2c and 2d illustrate the post-catalyst-loading adsorption–desorption isotherms and pore size distribution curves. The most significant changes in average pore size and pore volume were observed in AC after loading, with reductions of 19% and 22%, respectively. These changes are likely owing to the agglomeration of Ru active metal atoms within the AC pores, which blocked some micropores. Similarly, the extent of changes observed in Ru/AC-G surpassed those observed in AC-N and AC-GN. Thus, consistent with initial observations, the carriers AC-N and AC-GN were more conducive to the dispersion of the Ru active metal atoms.

Table 1. Textural Properties of Various Carriers and Catalysts

Sample	Average pore size (nm)	S_{BET} (m^2 g^{-1})	Pore volume (cm^3 g^{-1})
AC	3.06	591	0.45
AC-N	2.66	750	0.49
AC-G	2.56	520	0.37
AC-GN	2.82	591	0.39
Ru/AC	2.47	546	0.35
Ru/AC-N	2.66	678	0.47
Ru/AC-G	2.92	504	0.36
Ru/AC-GN	2.76	564	0.37

Note: S_{BET} : Brunauer-Emmett-Teller (BET) specific surface area

The SEM and TEM analyses were performed to characterize the morphologies of the carriers and catalysts. Large pores and mesopores were observed, as depicted in Fig. 3 parts a and b. The introduction of urea for nitrogen doping resulted in the generation of radicals at elevated temperatures, thereby etching the carbon carrier, consistent with the BET results. Carbon deposition on the surface and within the large pores of AC-GN is revealed in Fig. 3c. This occurred owing to the dehydration of glucose during the hydrothermal process at 180 °C, gradually separating from the solution to form an aqueous emulsion. Further dehydration of the sugar resulted in the formation of oligomeric nuclei within the sugar micelles, which subsequently grew into nanoscale spheres (Sakaki *et al.* 1996; Xu *et al.* 2008). These carbon microspheres, deposited on the carbon surface and further carbonized at 800 °C, were not observed in AC-GN. As depicted in Fig. 3d, the TEM analysis of AC-GN clearly revealed micro and mesoporous structures, confirming that the carbonization of glucose did not lead to the blockage of the micro and mesopores. The energy-dispersive spectroscopy (EDS) elemental distribution map (Fig. 3e) indicated the doping of nitrogen atoms into the aromatic carbon framework, with Ru nanoparticles being uniformly dispersed on the AC-GN carrier. Furthermore, graphitic carbon lattice fringes and Ru nanoparticles with a lattice spacing of 0.206 nm, corresponding to the Ru (101) plane, are evident in Fig. 3f-h (Agarwal and Ganguli 2014). In addition, the electron

diffraction patterns revealed two distinct diffraction rings, corresponding to the (002) and (101) planes of graphitic carbon and Ru, respectively (Wang *et al.* 2023a).
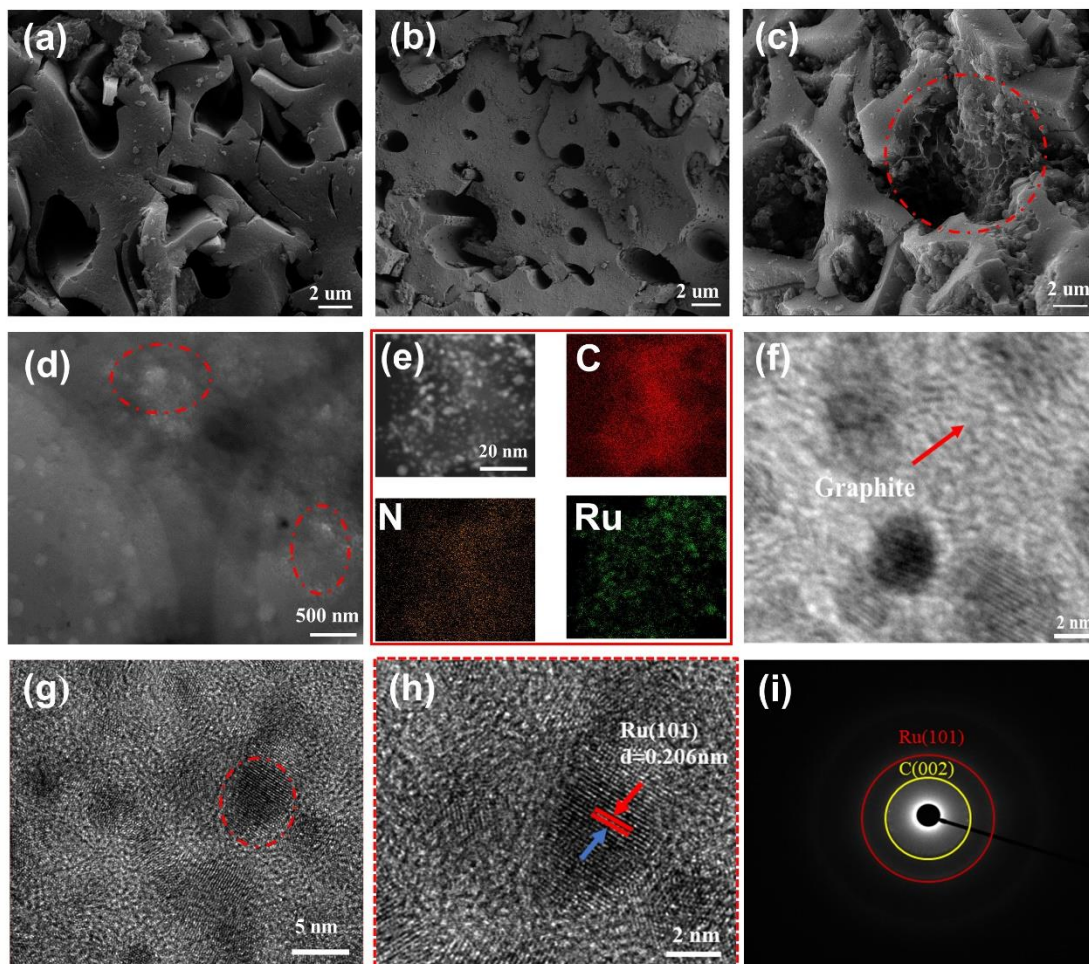

Fig. 3. SEM images of AC (a), AC-N (b), and AC-GN (c). TEM images of AC-GN (d). EDS elemental mapping of Ru/AC-GN (e). High-resolution transmission electron microscopy image of Ru/AC-GN (f-h). SAED pattern of Ru/AC-GN.

The XRD was used to analyze the carbon crystalline structures and the metallic Ru crystalline structures of the four Ru-based catalysts. A prominent diffraction peak near 26° was observed for all the catalysts, as shown in Fig. 4a (Kulkarni *et al.* 2017). This peak is attributed to the (002) diffraction of graphitic carbon. There was no considerable difference in the diffraction peak at 26° between Ru/AC and Ru -N, indicating that the hydrothermal post-treatment nitrogen doping process had a minimal impact on the crystalline structure of the carbon. The diffraction peaks observed for Ru/AC-G and Ru/AC-GN were less intense and broader than those for AC and AC-N, signifying a slight variation in the crystallinity of the carbon carrier. This suggests that the nitrogen-doped carbon generated from the glucose–urea mixture was successfully deposited on the AC surface and underwent carbonization at 800 °C. Notably, distinct absorbance peaks corresponding to the Ru (101) plane were observed for Ru/AC and Ru/AC-G near 43°, while similar peaks were not observed for Ru/AC-G and Ru/AC-GN, in contrast with the TEM results(Tee *et al.* 2015). This discrepancy was attributed to the uniform dispersion of Ru nanoparticles on the AC-N and AC-GN carriers (Wen *et al.* 2018). Raman spectroscopy was employed

to further analyze the graphitization degree of the four carbon carriers, as illustrated in Fig. 4b. Peaks were noted near 1345 cm^{-1} (D band) and 1575 cm^{-1} (G band), with a lower D to G band intensity ratio (I_D: I_G) indicating a higher level of graphitization (Odedairo *et al.* 2014). AC exhibited the lowest I_D: I_G ratio of 1.05, signifying the highest degree of graphitization. In the case of AC-N, the I_D: I_G ratio was 1.12, suggesting a reduction in graphitization owing to the disruption of carbon chains by nitrogen doping. Furthermore, AC-G exhibited an I_D: I_G value of 1.14, revealing that the hydrothermal carbon was graphitized at 800 °C, consistent with the XRD results. AC-GN displayed the highest I_D: I_G ratio of 1.23 among the carriers, indicating the lowest degree of graphitization and an increased number of defect structures. This is a consequence of the combined effects of the disruption of carbon chains by nitrogen atom doping and the deposition of nitrogen-doped carbon on the AC surface.
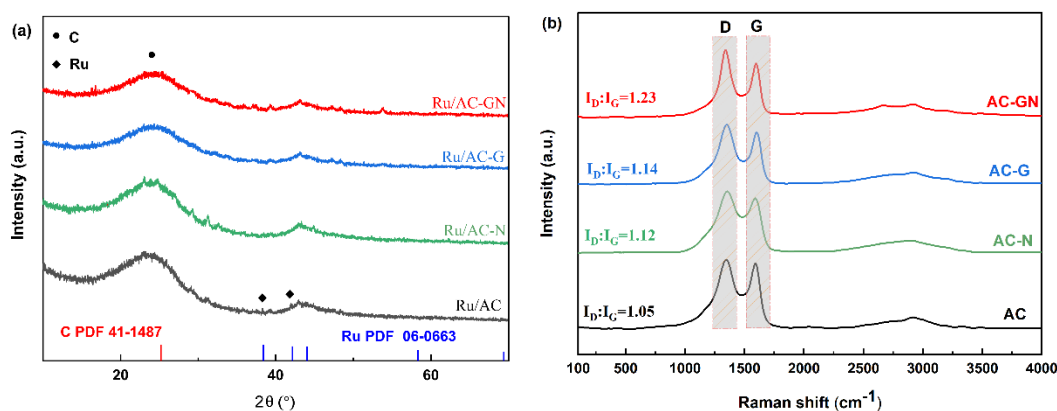

Fig. 4. XRD patterns of the catalyst samples (a) and Raman patterns of the support samples (b)

Table 2 presents the elemental analysis results of the different carbon carriers. The results indicate that the respective nitrogen contents in AC and AC-G, which were not doped with urea, were only 0.5 and 0.4 wt%. Upon the addition of urea alone, the nitrogen content increased to 1.8 wt%. This is because the generation of ammonia at high temperatures led to the formation of NH_2, NH, and N radicals, thereby doping N atoms into the aromatic carbon framework. In AC-GN, the nitrogen content rose to 4.7 wt%, indicating that glucose addition not only facilitated the doping of N atoms into the highly aromatic carbon framework but also generated new nitrogen-doped carbon deposits on the AC surface, achieving *in situ* nitrogen doping. Notably, compared to traditional post-treatment nitrogen doping methods, this method resulted in increased nitrogen doping. The thermal stability of the carriers, a critical factor affecting ammonia decomposition catalyst activity at reaction temperatures between 400 and 550 °C, was determined through TG. The TG curves of the four carbon carriers (Fig. 5a) exhibited similar weight loss profiles, with varying degrees of loss before 200 °C, primarily due to the vaporization of water. For AC-G and AC-GN, slight mass loss was observed between 500 and 600 °C. Ultimately, the mass loss for AC and AC-G was within 1%, while that for AC-G and AC-GN was approximately 2%, presumed to be caused by the decomposition of certain unstable structures generated by glucose carbonization at high temperatures(Liu *et al.* 2020). Given that the optimal reaction temperature for Ru/AC-GN in ammonia decomposition is around 500 °C, AC-GN possesses adequate thermal stability.

Table 2. Summary of the Elemental Analysis Results of the Various Carriers

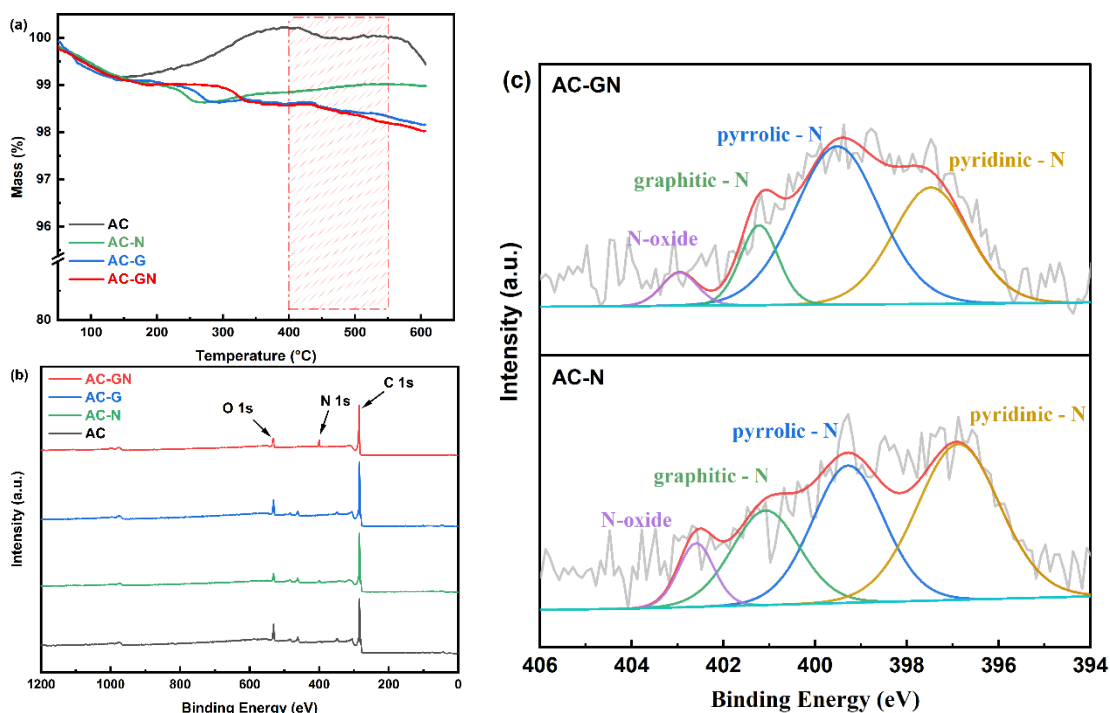| Sample	Content (wt%)			
	C	H	N	O (Calculated)
AC	88.0	0.6	0.5	10.9
AC-N	88.8	0.6	1.8	8.8
AC-G	89.9	0.3	0.4	9.4
AC-GN	89.4	0.4	4.7	5.5

Fig. 5. Mass loss of various carrier composites as a function of temperature between 50 and 600 °C, measured with a heating rate of 10 °C/min under a nitrogen atmosphere (a). XPS survey spectra of AC-N, AC-N, AC-G, and AC-GN (b). XPS N1s spectra of AC-N and AC-GN (c)

X-ray photoelectron spectroscopy (XPS) was employed to investigate the elemental composition and chemical bonds of the carriers. The XPS spectra of the Ru/AC-N and Ru/AC-GN samples revealed deconvoluted peaks attributed to C 1s, N 1s, and O 1s (Fig. 5b)(Yu *et al.* 2014). By contrast, Ru/AC and Ru/AC-G lacked a peak corresponding to N 1s, and the N1S peak was substantially higher in AC-GN, consistent with the elemental analysis results. The high-resolution N1s peak in Fig. 5c revealed the presence of pyridinic-N, pyrrolic-N, graphitic-N, and oxide-N (Han *et al.* 2019). Nitrogen species play a crucial role in the performance of the carriers, as shown in Table S1, which displays the content of nitrogen species in the catalysts obtained from the two nitrogen doping methods. Notably, the highest pyridinic-N and pyrrolic-N contents were observed in Ru/AC-N and Ru/AC-GN, respectively. Furthermore, Ru/AC-GN exhibited a higher content of pyrrolic-N compared to Ru/AC-N, while Ru/AC-N had a higher pyridinic-N content. Studies have indicated that pyridinic-N and pyrrolic-N can serve as effective sites for active metals, enhancing the dispersion of active metal components and facilitating the binding between metallic Ru and nitrogen-doped carbon carriers (Zhong and Aika 1998). However, the mechanism of action of these two nitrogen species remains unclear (Miao *et al.* 2017;

Wang *et al.* 2023b). With increasing pyrolysis temperature, the pyridinic-N content decreased gradually, transforming into pyrrolic and graphitic nitrogen. Excessive pyridinic-N appears unsuitable for high-temperature ammonia decomposition systems. Therefore, the AC-GN carrier, with high pyrrolic-N and graphitic-N contents, is deemed more suitable.

Structure–Activity Relationship between Carriers and Active Metals

Currently, there exists a consensus regarding the mechanism of NH_3 decomposition on active metal surfaces, which can be delineated into eight steps (Fig. 6). These steps encompass ammonia adsorption, dissociation, and the formation and desorption of decomposition products (Chen *et al.* 2021; Su *et al.* 2024). Initially, gaseous $NH_3(g)$ adsorbs on the active sites of the catalyst(ad), generating adsorbed $NH_3(ad)$ (step 1). Subsequently, $NH_3(ad)$ dehydrogenates to produce adsorbed N(ad) and H(ad) (steps 2 to 4). Eventually, N(ad) and H(ad) combine to form adsorbed $N_2(ad)$ and $H_2(ad)$ (steps 5 to 6), respectively, which subsequently desorb to yield gaseous $N_2(g)$ and $H_2(g)$ (steps 7 and 8). However, the rate-limiting step remains a subject of debate. Enhanced Ru nanoparticle dispersion facilitates the conversion of reaction gases between gaseous and adsorbed states (step 1) or from adsorbed states back to gaseous states (steps 7 and 8). Moreover, the efficiency of gas transport also influences the aforementioned reaction process, necessitating the provision of more anchoring sites and a porous structure in the carrier.
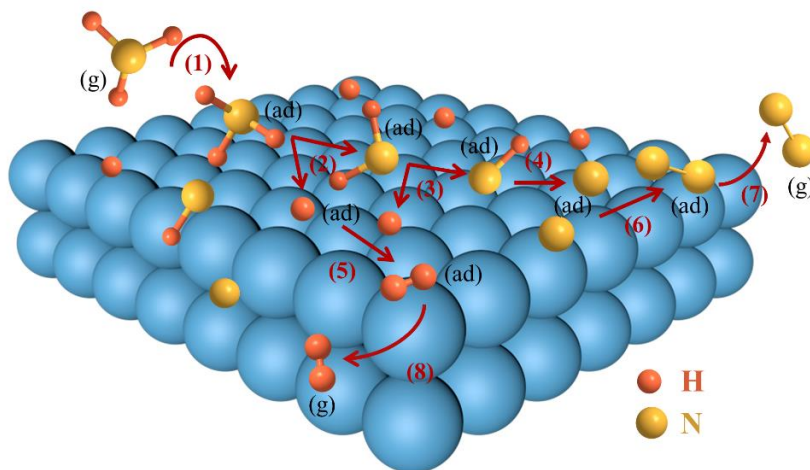

Fig. 6. Schematic of NH_3 decomposition reaction in the presence of Ru catalyst

As previously mentioned, the nitrogen-doped carbon structures deposited in AC-GN predominantly reside on the outer surface and within large pores, preserving a hierarchical porous structure conducive to gas transport. Additionally, the outer surface and large pores of AC-GN offer more defect sites, conducive to anchoring Ru, thereby enhancing its dispersion and stability. Wu *et al.* (2023) found that active metals loaded on the outer surface of the carrier exhibit superior ammonia decomposition performance, attributed to the ease of gas adsorption–desorption on the outer surface. Consequently, Ru situated on the outer surface and large pores of AC-GN would theoretically enhance the overall catalytic performance. The gradual dissociation of $NH_3(ad)$ (3-5) also plays a pivotal role in influencing the catalytic reaction. Wang *et al.* (2023b) observed that the electron density on the outer surface of CNTs surpasses that on the inner surface, resulting

in heightened activity of the active metals loaded on the outer surface. The introduction of N alters the electron distribution of C, inducing electron-rich states and enhancing the electron transfer capability. Furthermore, AC-GN retains its original degree of graphitization, accompanied by a notable improvement in the electrical conductivity of its outer surface, thereby facilitating the dissociation of $NH_3(ad)$.

To determine the dispersion of Ru nanoparticles on the carrier, the diameters of at least 50 Ru particles were analyzed statistically. Figure S2 presents TEM images of three catalysts, namely Ru/AC, Ru/AC-N, and Ru/AC-GN, with Ru nanoparticle diameters of 3.39, 2.98, and 2.79 nm, respectively. The Ru nanoparticles in Ru/AC-GN exhibited the smallest diameter and the most optimal dispersion. To further elucidate the presence of the active metal Ru on AC-N and AC-GN compared to AC, Ru 3p spectra were deconvoluted and fitted. Figure 7a-c illustrates two main peaks corresponding to $Ru3p^{3/2}$ and $Ru3p^{1/2}$. The peaks near 462.4 and 484.7 eV correspond to Ru^0, whereas those at 464.4 and 486.7 eV correspond to Ru^{n+} (Tang *et al.* 2015; Wang *et al.* 2018). The relative contents of Ru^0 and Ru^{n+} were determined based on the peak areas (Fig. 7d). The Ru^0 contents of Ru/AC, Ru/AC-N, and Ru/AC-GN were found to be 50%, 70%, and 74%, respectively, indicating that the Ru^0 content increases with nitrogen content. This demonstrates that nitrogen doping can regulate the electron cloud density of the carbon carrier, thereby enhancing electron transfer between the metal and carrier. Consequently, electron transfer occurs between N atoms and metallic Ru in Ru/AC-N and Ru/AC-GN, resulting in higher Ru^0 content. Notably, among the four carriers, AC-GN exhibited the greatest performance.
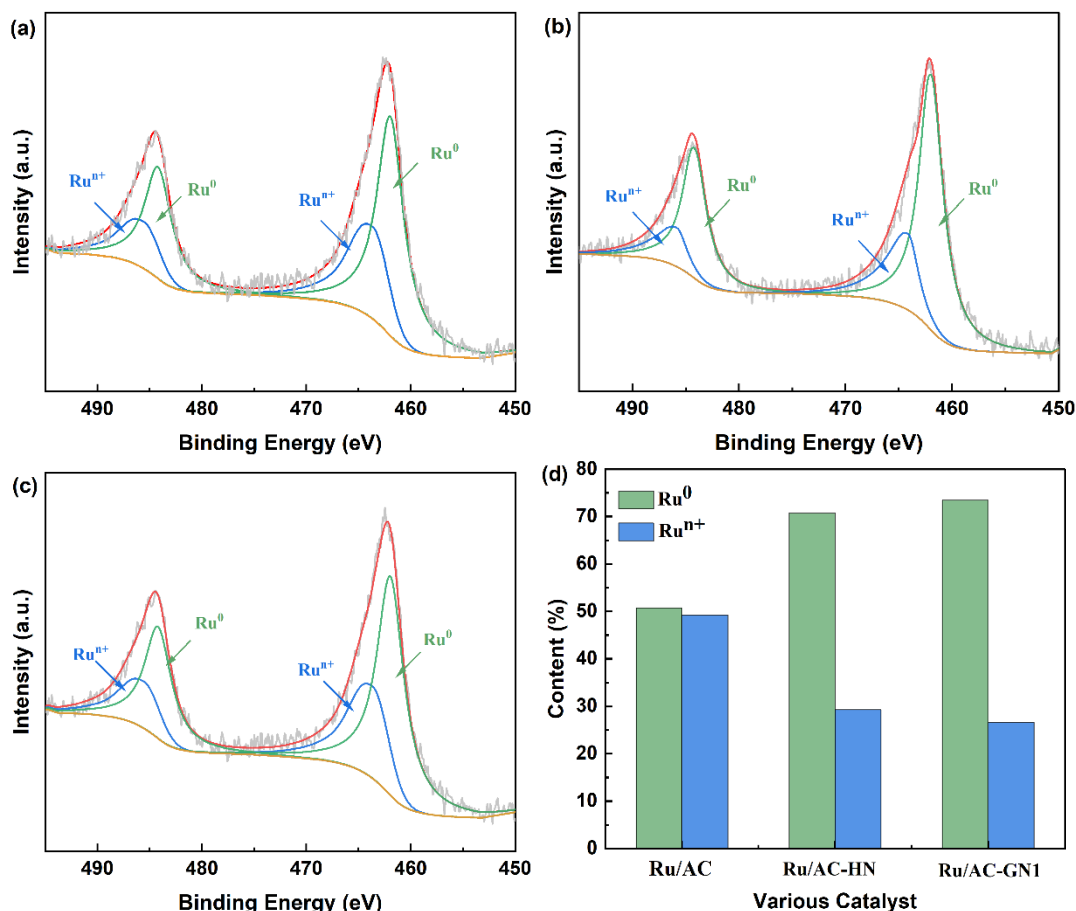

Fig. 7. Ru 3p XPS spectra of Ru/AC (a), Ru/AC-N (b), Ru/AC-GN (c), and Ru^0 and Ru^{n+} contents of various catalysts (d)

The H_2-TPR curves of the unreduced catalysts indicated that 300 °C is a suitable reduction temperature for Ru (Fig. 8a). Excessively high reduction temperatures might result in Ru particle agglomeration, while temperatures below 300 °C might not effectively reduce Ru oxides to Ru. In the H_2-TPR spectra, the peaks observed for Ru/AC-GN showed an increase of approximately 10 °C compared to Ru/AC-N, a consequence of the interactions between the nitrogen-doped carriers and Ru oxides, which intensified with increased nitrogen content (Chen *et al.* 2017). Such metal–carrier interactions prevent Ru nanoparticle agglomeration. Furthermore, the issue of catalyst poisoning is crucial to the study of catalyst performance. It has been reported that Ru-based catalysts are primarily affected by hydrogen poisoning in ammonia synthesis reactions (Lin *et al.* 2021), while activated carbon carriers may generate gases such as CO_X (CO, CO_2) at high temperatures. Due to the porous nature of activated carbon, these CO_X and H_2 molecules excessively adsorb on the catalyst surface, occupying active sites and thereby inhibiting or hindering the catalytic reaction (Chen *et al.* 2024). Since the treatment temperature of activated carbon (800 °C) is much higher than the temperature of ammonia decomposition reactions, unstable oxygen-containing functional groups are decomposed in advance, making the impact of CO on the catalyst negligible. Ren and others have studied the desorption behavior of hydrogen on catalysts through H_2-TPD, finding that hydrogen begins to desorb at approximately 100 °C and is essentially fully desorbed by around 200 °C (Ren *et al.* 2017). Under the conditions of ammonia decomposition reactions at 400 to 500 °C, hydrogen desorbs more readily. This suggests that nitrogen may have a more significant impact on catalyst performance in ammonia decomposition reactions. Current research considers nitrogen desorption as the rate-controlling step in ammonia decomposition on Ru catalysts (Zhang *et al.* 2014). The N_2-TPD curves exhibited three peaks (Fig. 8b) near 140, 450, and 720 °C. The desorption peak at 140 °C, attributed to the physical desorption of N_2 from the carbon surface and pores, suggests that the other two peaks at higher temperatures correspond to deep pore desorption and chemical adsorption. Ru/AC-GN desorbed N_2 primarily between 400 and 500 °C, whereas Ru/AC-N displayed a minor peak after 700 °C. This is possibly owing to the larger surface area and smaller average pore size of AC-N, leading to greater N_2 desorption resistance in the pores of Ru/AC-N. It is anticipated that Ru loaded on AC-GN will demonstrate superior NH_3 decomposition performance.
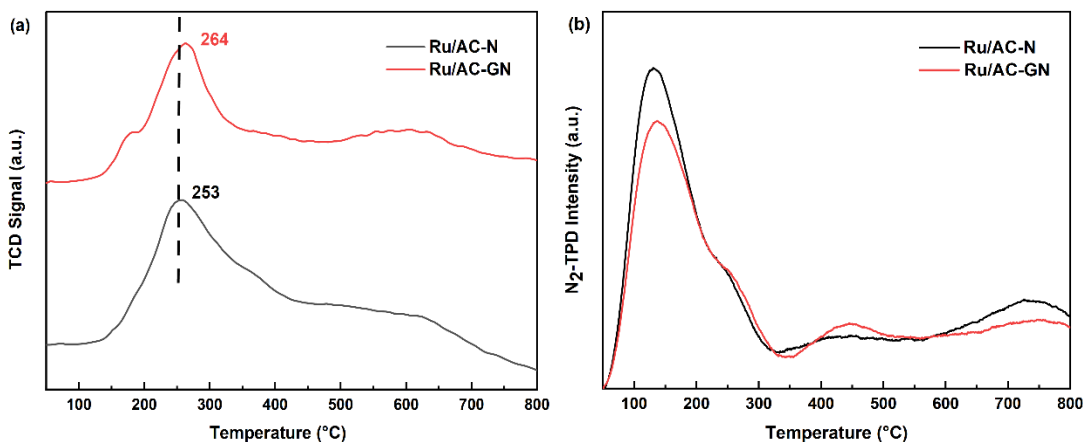

Fig. 8. H_2-TPR (a) and N_2-TPD (b) profiles of the catalysts fabricated in this study

Assessment of NH_3 Decomposition Performance

Figure 9a demonstrates that the NH_3 conversion rates of the four catalysts exhibit a direct correlation with temperature. NH_3 decomposition is an endothermic reaction. Therefore, the NH_3 conversion rate rises with increasing reaction temperature (Wu *et al.* 2023). Among the four catalysts, Ru/AC-GN displayed the highest activity, followed by Ru/AC-N, whereas Ru/AC and Ru/AC-G showed no significant difference in activity. Notably, within the low-temperature range of 425 to 500 °C, Ru/AC-GN exhibited a markedly superior conversion efficiency compared to the other catalysts. At a gas hourly space velocity (GHSV) of 15000 mL g_{cat}^{-1} h^{-1}, Ru/AC-GN achieved 69% NH_3 conversion at 475 °C, corresponding to an H_2 generation rate of 11.5 mmol g_{cat}^{-1} min^{-1} (Table S2). Moreover, at 525 °C, it achieved 94% NH_3 conversion, equivalent to an H_2 generation rate of 15.8 mmol g_{cat}^{-1} min^{-1}. Figure 9b presents Arrhenius plots illustrating the logarithm of the H_2 formation rate *versus* the reciprocal of the absolute temperature. The determined apparent activation energies (Ea) for Ru/AC, Ru/AC-N, and Ru/AC-GN were 78.13, 61.80 and 60.28 kJ mol^{-1}, respectively. As previously discussed, the dispersion of Ru on the outer surface and large pores of AC-GN facilitated higher gas adsorption–desorption rates, resulting in the lowest E_a and high activity at low temperatures in the case of Ru/AC-GN. Compared with previously reported Ru-based carbon-supported NH_3 decomposition catalysts (Table S3), the performance of Ru/AC-GN is significantly superior, and it is comparable to the high-performing MgO, offering a cost-effective alternative through the valorization of biomass resources (Wang *et al.* 2004; Lucentini *et al.* 2019).
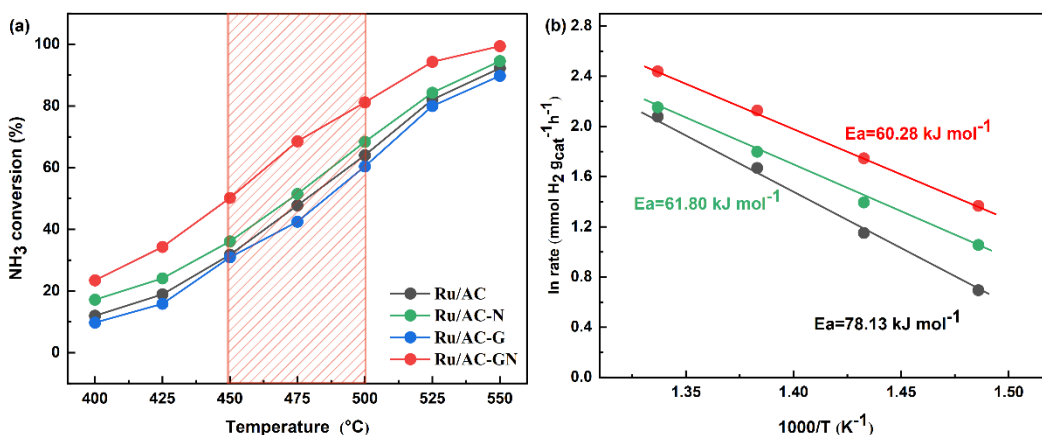

Fig. 9. NH_3 conversion in the presence of various catalysts at a GHSV of 15000 mL g_{cat}^{-1} h^{-1} (a) and the Arrhenius plots obtained between 400 and 475 ℃ (b)

The catalytic stability of Ru/AC-GN for NH_3 decomposition was evaluated at 500 °C with a GHSV of 15000 mL g_{cat}^{-1} h^{-1}. Over a 24 h reaction period, Ru/AC-N and Ru/AC-GN demonstrated substantially better stability than Ru/AC (Fig. 10a), with Ru/AC-GN exhibiting particularly notable effects owing to the interactions between the nitrogen-doped structures and Ru within the outer surface and large pores of the AC-GN carrier. The XRD patterns in Fig. 10b show no significant change in Ru size after 24 h of durability testing. However, the stability of the Ru/AC-GN catalyst must be further improved. The addition of a second metal or promoters could further enhance the low-temperature activity of the catalyst and reduce the reaction temperature, thereby extending the catalyst lifespan.
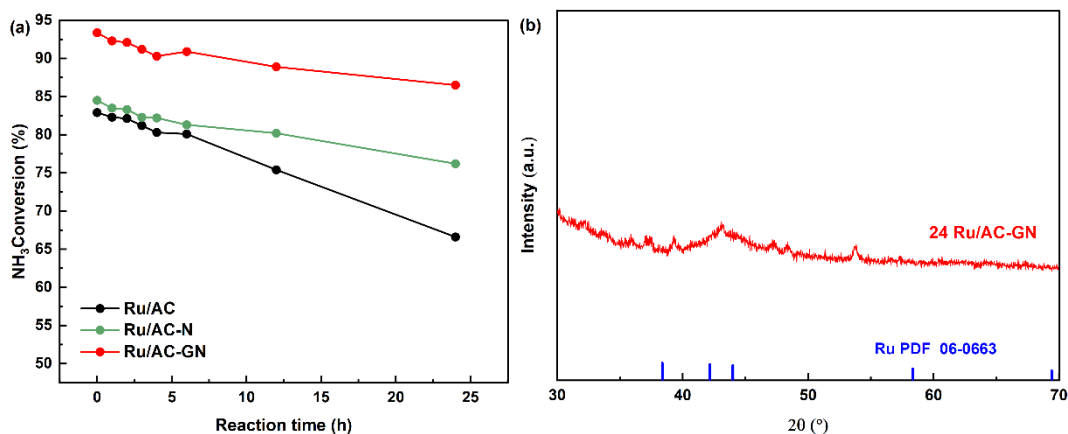
Fig. 10. Stability test results of various catalysts for NH_3 decomposition at 500 ℃ with a GHSV of 15000 mL g_{cat}^{-1} h^{-1} (a), and XRD patterns of the aged catalyst samples (b)

CONCLUSIONS

1. Nitrogen-doped composite materials were successfully synthesized *via* a hydrothermal pyrolysis method. Unlike conventional nitrogen doping techniques, this approach not only introduces N atoms into carbon chains but also deposits nitrogen-containing carbon materials on the surface and within the large pores of AC.

2. By incorporating glucose, *in situ* nitrogen doping was achieved, boosting the nitrogen content of the carbon carrier while preserving its hierarchical pore structure and degree of graphitization.

3. This methodology improved the effective dispersion of Ru nanoparticles on the external surface and within the large pores of the carrier, enhancing electron transfer capabilities. Leveraging of the inherent advantage of easier gas adsorption–desorption on the external surface of the catalyst, the low-temperature activity of the catalyst was increased in this study.

4. Examination of nitrogen species revealed that nitrogen doping enhanced metal–carrier interactions, effectively improving the thermal stability of the catalyst. The relatively stable pyrrolic and graphitic nitrogen were more suitable for the ammonia decomposition reaction.

5. Finally, catalytic performance tests demonstrated that the Ru/AC-GN catalyst exhibited outstanding activity and catalytic stability for NH_3 decomposition, notably surpassing other carbon-supported Ru catalysts at low temperatures. This nitrogen doping method in AC, characterized by relatively high nitrogen doping levels, excellent hierarchical pore structures, and superior catalytic performance, provides valuable insights into the design and preparation of catalyst carriers for ammonia decomposition reactions.

ACKNOWLEDGEMENTS

REFERENCES CITED

Abe, J. O., Popoola, A. P. I., Ajenifuja, E., and Popoola, O. M. (2019). "Hydrogen energy, economy and storage: Review and recommendation," *International Journal of Hydrogen Energy* 44(29), 15072-15086. DOI: 10.1016/j.ijhydene.2019.04.068

Agarwal, S., and Ganguli, J. N. (2014). "Hydrogenation by nanoscale ruthenium embedded into the nanopores of K-10 clay," *RSC Advances* 4(23), article 11893. DOI: 10.1039/c3ra47162d

Calzaferri, G., Gallagher, S. H., Lustenberger, S., Walther, F., and Brühwiler, D. (2023). "Multiple equilibria description of type H1 hysteresis in gas sorption isotherms of mesoporous materials," *Materials Chemistry and Physics* 296, article 127121. DOI: 10.1016/j.matchemphys.2022.127121

Cao, C.-F., Wu, K., Zhou, C., Yao, Y.-H., Luo, Y., Chen, C.-Q., Lin, L., and Jiang, L. (2022). "Electronic metal-support interaction enhanced ammonia decomposition efficiency of perovskite oxide supported ruthenium," *Chemical Engineering Science* 257, article 117719. DOI: 10.1016/j.ces.2022.117719

Chang, F., Gao, W., Guo, J., and Chen, P. (2021). "Emerging materials and methods toward ammonia-based energy storage and conversion," *Advanced Materials* 33(50), article 2005721. DOI: 10.1002/adma.202005721

Chen, C., Wu, K., Ren, H., Zhou, C., Luo, Y., Lin, L., Au, C., and Jiang, L. (2021). "Ru-based catalysts for ammonia decomposition: A mini-review," *Energy & Fuels* 35(15), 11693-11706. DOI: 10.1021/acs.energyfuels.1c01261

Chen, L., Li, Y., Zhang, X., Zhang, Q., Wang, T., and Ma, L. (2017). "Effect of Ru particle size on hydrogenation/decarbonylation of propanoic acid over supported Ru catalysts in aqueous phase," *Catalysis Letters* 147(1), 29-38. DOI: 10.1007/s10562-016-1877-4

Chen, S.-Y., Wang, L.-Y., Chen, K.-C., Yeh, C.-H., Hsiao, W.-C., Chen, H.-Y., Nishi, M., Keller, M., Chang, C.-L., Liao, C.-N., Mochizuki, T., Chen, H.-Y. T., Chou, H.-H., and Yang, C.-M. (2024). "Ammonia synthesis over cesium-promoted mesoporous-carbon-supported ruthenium catalysts: Impact of graphitization degree of the carbon support," *Applied Catalysis B: Environment and Energy* 346, article 123725. DOI: 10.1016/j.apcatb.2024.123725

Du, H.-G., Zhang, X.-F., Ding, L.-W., Liu, J.-L., Yu, L.-H., Zhang, X.-H., Dou, Y., Cao, L.-M., Zhang, J., and He, C.-T. (2024). "Engineering pore-size distribution of metal-loaded carbon catalysts by in situ cavitation for boosting electrochemical mass transfer," *Applied Catalysis B: Environmental* 342, article 123396. DOI: 10.1016/j.apcatb.2023.123396

Han, F., Liu, Z., Jia, J., Ai, J., Liu, L., Liu, J., and Wang, Q.-D. (2019). "Influences of N species in N-doped carbon carriers on the catalytic performance of supported Pt," *Materials Chemistry and Physics* 237, article 121881. DOI: 10.1016/j.matchemphys.2019.121881

Hien, N., Kim, H., Jeon, M., Lee, J., Ridwan, M., Tamarany, R., and Yoon, C. (2015). "Ru-N-C Hybrid nanocomposite for ammonia dehydrogenation: Influence of N-doping on catalytic activity," *Materials* 8(6), 3442-3455. DOI: 10.3390/ma8063442

Karim, A. M., Prasad, V., Mpourmpakis, G., Lonergan, W. W., Frenkel, A. I., Chen, J. G., and Vlachos, D. G. (2009). "Correlating particle size and shape of supported Ru/γ-Al_2O_3 catalysts with NH_3 decomposition activity," *Journal of the American Chemical Society* 131(34), 12230-12239. DOI: 10.1021/ja902587k

Kulkarni, G., Velhal, N., Phadtare, V., and Puri, V. (2017). "Enhanced electromagnetic interference shielding effectiveness of chemical vapor deposited MWCNTs in X-band region," *Journal of Materials Science: Materials in Electronics* 28(10), 7212-7220. DOI: 10.1007/s10854-017-6402-z

Lee, Y.-J., Cha, J., Kwak, Y., Park, Y., Jo, Y. S., Jeong, H., Sohn, H., Yoon, C. W., Kim, Y., Kim, K.-B., and Nam, S. W. (2021). "Top-down syntheses of nickel-based structured catalysts for hydrogen production from ammonia," *ACS Applied Materials & Interfaces*, 13(1), 597-607. DOI: 10.1021/acsami.0c18454

Lin, B., Wu, Y., Fang, B., Li, C., Ni, J., Wang, X., Lin, J., and Jiang, L. (2021). "Ru surface density effect on ammonia synthesis activity and hydrogen poisoning of ceria-supported Ru catalysts," *Chinese Journal of Catalysis* 42(10), 1712-1723. DOI: 10.1016/S1872-2067(20)63787-1

Liu, H., Chen, B., and Wang, C. (2020). "Pyrolysis kinetics study of biomass waste using shuffled complex evolution algorithm," *Fuel Processing Technology* 208, article 106509. DOI: 10.1016/j.fuproc.2020.106509

Liu, S., Sun, J., and Huang, Z. (2010). "Carbon spheres/activated carbon composite materials with high Cr(VI) adsorption capacity prepared by a hydrothermal method," *Journal of Hazardous Materials* 173(1), 377-383. DOI: 10.1016/j.jhazmat.2009.08.086

Lucentini, I., Casanovas, A., and Llorca, J. (2019). "Catalytic ammonia decomposition for hydrogen production on Ni, Ru and Ni Ru supported on CeO_2," *International Journal of Hydrogen Energy* 44(25), 12693-12707. DOI: 10.1016/j.ijhydene.2019.01.154

Luo, Y., Yang, Q., Nie, W., Yao, Q., Zhang, Z., and Lu, Z.-H. (2020). "Anchoring IrPdAu nanoparticles on NH_2-SBA-15 for fast hydrogen production from formic acid at room temperature," *ACS Applied Materials & Interfaces* 12(7), 8082-8090. DOI: 10.1021/acsami.9b16981

Mehrpooya, M., and Habibi, R. (2020). "A review on hydrogen production thermochemical water-splitting cycles," *Journal of Cleaner Production* 275, artcile 123836. DOI: 10.1016/j.jclepro.2020.123836

Miao, H., Li, S., Wang, Z., Sun, S., Kuang, M., Liu, Z., and Yuan, J. (2017). "Enhancing the pyridinic N content of nitrogen-doped graphene and improving its catalytic

activity for oxygen reduction reaction," *International Journal of Hydrogen Energy* 42(47), 28298-28308. DOI: 10.1016/j.ijhydene.2017.09.138

Mukherjee, S., Devaguptapu, S. V., Sviripa, A., Lund, C. R. F., and Wu, G. (2018). "Low-temperature ammonia decomposition catalysts for hydrogen generation," *Applied Catalysis B: Environmental* 226, 162-181. DOI: 10.1016/j.apcatb.2017.12.039

Nagaoka, K., Eboshi, T., Abe, N., Miyahara, S., Honda, K., and Sato, K. (2014). "Influence of basic dopants on the activity of Ru/Pr_6O_{11} for hydrogen production by ammonia decomposition," *International Journal of Hydrogen Energy* 39(35), 20731-20735. DOI: 10.1016/j.ijhydene.2014.07.142

Nakamura, I., Kubo, H., and Fujitani, T. (2022). "Critical role of Cs doping in the structure and NH_3 decomposition performance of Ru/MgO catalysts," *Applied Catalysis A: General* 644, article 118806. DOI: 10.1016/j.apcata.2022.118806

Odedairo, T., Ma, J., Gu, Y., Chen, J., Zhao, X. S., and Zhu, Z. (2014). "One-pot synthesis of carbon nanotube–graphene hybrids via syngas production," *J. Mater. Chem. A* 2(5), 1418-1428. DOI: 10.1039/C3TA13871B

Rarogpilecka, W., Miskiewicz, E., Szmigiel, D., and Kowalczyk, Z. (2005). "Structure sensitivity of ammonia synthesis over promoted ruthenium catalysts supported on graphitised carbon," *Journal of Catalysis* 231(1), 11-19. DOI: 10.1016/j.jcat.2004.12.005

Raróg-Pilecka, W., Szmigiel, D., Komornicki, A., Zieliński, J., and Kowalczyk, Z. (2003). "Catalytic properties of small ruthenium particles deposited on carbon," *Carbon* 41(3), 589-591. DOI: 10.1016/S0008-6223(02)00393-7

Ren, R., Dou, B., Zhang, H., Wu, K., Wang, Y., Chen, H., and Xu, Y. (2023). "Syngas production from CO_2 reforming of glycerol by mesoporous Ni/CeO_2 catalysts," *Fuel* 341, article 127717. DOI: 10.1016/j.fuel.2023.127717

Ren, S., Huang, F., Zheng, J., Chen, S., and Zhang, H. (2017). "Ruthenium supported on nitrogen-doped ordered mesoporous carbon as highly active catalyst for NH_3 decomposition to H_2," *International Journal of Hydrogen Energy* 42(8), 5105-5113. DOI: 10.1016/j.ijhydene.2016.11.010

Rodríguez-reinoso, F. (1998). "The role of carbon materials in heterogeneous catalysis," *Carbon*, 36(3), 159-175. DOI: 10.1016/S0008-6223(97)00173-5

Sakaki, T., Shibata, M., Miki, T., Hirosue, H., and Hayashi, N. (1996). "Decomposition of cellulose in near-critical water and fermentability of the products," *Energy & Fuels* 10(3), 684-688. DOI: 10.1021/ef950160+

Stöhr, B., Boehm, H. P., and Schlögl, R. (1991). "Enhancement of the catalytic activity of activated carbons in oxidation reactions by thermal treatment with ammonia or hydrogen cyanide and observation of a superoxide species as a possible intermediate," *Carbon* 29(6), 707-720. DOI: 10.1016/0008-6223(91)90006-5

Su, Z., Guan, J., Liu, Y., Shi, D., Wu, Q., Chen, K., Zhang, Y., and Li, H. (2024). "Research progress of ruthenium-based catalysts for hydrogen production from ammonia decomposition," *International Journal of Hydrogen Energy* 51, 1019-1043. DOI: 10.1016/j.ijhydene.2023.09.107

Sun, S., Jiang, Q., Zhao, D., Cao, T., Sha, H., Zhang, C., Song, H., and Da, Z. (2022). "Ammonia as hydrogen carrier: Advances in ammonia decomposition catalysts for promising hydrogen production," *Renewable and Sustainable Energy Reviews* 169, article 112918. DOI: 10.1016/j.rser.2022.112918

Tan, H., Li, K., Sioud, S., Cha, D., Amad, M. H., Hedhili, M. N., and Al-Talla, Z. A. (2012). "Synthesis of Ru nanoparticles confined in magnesium oxide-modified

mesoporous alumina and their enhanced catalytic performance during ammonia decomposition," *Catalysis Communications* 26, 248-252. DOI: 10.1016/j.catcom.2012.06.007

Tang, M., Mao, S., Li, M., Wei, Z., Xu, F., Li, H., and Wang, Y. (2015). "RuPd alloy nanoparticles supported on N-doped carbon as an efficient and stable catalyst for benzoic acid hydrogenation," *ACS Catalysis* 5(5), 3100-3107. DOI: 10.1021/acscatal.5b00037

Tee, S. Y., Lee, C. J. J., Dinachali, S. S., Lai, S. C., Williams, E. L., Luo, H.-K., Chi, D., Andy Hor, T. S., and Han, M.-Y. (2015). "Amorphous ruthenium nanoparticles for enhanced electrochemical water splitting," *Nanotechnology* 26(41), article 415401. DOI: 10.1088/0957-4484/26/41/415401

Wan, Z., Tao, Y., Shao, J., Zhang, Y., and You, H. (2021). "Ammonia as an effective hydrogen carrier and a clean fuel for solid oxide fuel cells," *Energy Conversion and Management* 228, article 113729. DOI: 10.1016/j.enconman.2020.113729

Wang, J., Wei, Z., Mao, S., Li, H., and Wang, Y. (2018). "Highly uniform Ru nanoparticles over N-doped carbon: pH and temperature-universal hydrogen release from water reduction," *Energy & Environmental Science* 11(4), 800-806. DOI: 10.1039/C7EE03345A

Wang, S. J., Yin, S. F., Li, L., Xu, B. Q., Ng, C. F., and Au, C. T. (2004). "Investigation on modification of Ru/CNTs catalyst for the generation of COx-free hydrogen from ammonia," *Applied Catalysis B: Environmental* 52(4), 287-299. DOI: 10.1016/j.apcatb.2004.05.002

Wang, Z., Chen, X., Sun, Y., Hua, D., Yang, S., Sun, L., Li, T., and Chen, L. (2023a). "Co-pyrolysis induced strong metal-support interaction in N-doped carbon supported Ni catalyst for the hydrogenolysis of lignin," *Chemical Engineering Journal* 473, 145182. DOI: 10.1016/j.cej.2023.145182

Wang, Z., Chen, X., Xie, X., Yang, S., Sun, L., Li, T., Chen, L., and Hua, D. (2023b). "Synthesis of aromatic monomers via hydrogenolysis of lignin over nickel catalyst supported on nitrogen-doped carbon nanotubes," *Fuel Processing Technology* 248, article 107810. DOI: 10.1016/j.fuproc.2023.107810

Wen, G., Gu, Q., Liu, Y., Schlögl, R., Wang, C., Tian, Z., and Su, D. S. (2018). "Biomass-derived graphene-like carbon: Efficient metal-free carbocatalysts for epoxidation," *Angewandte Chemie International Edition* 57(51), 16898-16902. DOI: 10.1002/anie.201809970

Wu, Z.-W., Xiong, J., Wang, C.-W., and Qin, Y.-H. (2023). "Supporting high-loading Ni on SBA-15 as highly active and durable catalyst for ammonia decomposition reaction," *International Journal of Hydrogen Energy* 48(12), 4728-4737. DOI: 10.1016/j.ijhydene.2022.11.050

Xu, Y., Weinberg, G., Liu, X., Timpe, O., Schlögl, R., and Su, D. S. (2008). "Nanoarchitecturing of activated carbon: Facile strategy for chemical functionalization of the surface of activated carbon," *Advanced Functional Materials* 18(22), 3613-3619. DOI: 10.1002/adfm.200800726

Yao, L., Shi, T., Li, Y., Zhao, J., Ji, W., and Au, C.-T. (2011). "Core–shell structured nickel and ruthenium nanoparticles: Very active and stable catalysts for the generation of COx-free hydrogen via ammonia decomposition," *Catalysis Today* 164(1), 112-118. DOI: 10.1016/j.cattod.2010.10.056

Yin, S. F., Xu, B. Q., Zhou, X. P., and Au, C. T. (2004a). "A mini-review on ammonia decomposition catalysts for on-site generation of hydrogen for fuel cell applications,"

Applied Catalysis A: General 277(1–2), 1-9. DOI: 10.1016/j.apcata.2004.09.020

Yin, S.-F., Xu, B.-Q., Ng, C.-F., and Au, C.-T. (2004b). "Nano Ru/CNTs: A highly active and stable catalyst for the generation of COx-free hydrogen in ammonia decomposition," *Applied Catalysis B: Environmental* 48(4), 237-241. DOI: 10.1016/j.apcatb.2003.10.013

Yu, J., Guo, M., Muhammad, F., Wang, A., Zhang, F., Li, Q., and Zhu, G. (2014). "One-pot synthesis of highly ordered nitrogen-containing mesoporous carbon with resorcinol–urea–formaldehyde resin for CO_2 capture," *Carbon* 69, 502-514. DOI: 10.1016/j.carbon.2013.12.058

Zhang, H., Alhamed, Y. A., Al-Zahrani, A., Daous, M., Inokawa, H., Kojima, Y., and Petrov, L. A. (2014). "Tuning catalytic performances of cobalt catalysts for clean hydrogen generation via variation of the type of carbon support and catalyst post-treatment temperature," *International Journal of Hydrogen Energy* 39(31), 17573-17582. DOI: 10.1016/j.ijhydene.2014.07.183

Zheng, W., Zhang, J., Xu, H., and Li, W. (2007). "NH_3 decomposition kinetics on supported Ru clusters: Morphology and particle size effect," *Catalysis Letters* 119(3–4), 311-318. DOI: 10.1007/s10562-007-9237-z

Zhong, Z., and Aika, K. (1998). "The effect of hydrogen treatment of active carbon on Ru catalysts for ammonia synthesis," *Journal of Catalysis* 173(2), 535-539. DOI: 10.1006/jcat.1997.1943

APPENDIX
Supplementary

Appendix contains:
Section S1: Sample characterization (H_2-TPR and N_2-TPD)
Section S2: Catalyst Activity Tests
Table S1: N1s XPS analysis of various carbon materials.
Figure. S2: TEM images and Ru particle size distribution histograms of Ru/AC (a, d),
          Ru/AC-N (b, e) and Ru/AC-GN (c, f).
Table S2: H_2 formation rate (mmol min^{-1} g$^{-1}_{cat}$) for various catalysts.
Table S3 Catalytic activity of the supported Ru catalysts for NH_3 decomposition.

Section S1 Sample characterization (H_2-TPR and N_2-TPD)

For the H_2-TPR test, 50 mg of unreduced catalyst loaded in a U-shaped quartz tube was initially heated from room temperature to 100 °C at a heating rate of 10 °C min^{-1} and held at 100 °C for 1 h in an Ar gas flow (50 mL min^{-1}) to remove impurities such as water. Subsequently, it was heated from 50 to 800 °C at a rate of 10 °C min^{-1} in a 10% H_2/Ar gas flow (50 mL min^{-1}), and the amount of H_2 consumed during this heating process was recorded using a thermal conductivity detector (TCD).

For the N_2-TPD test, 50 mg of reduced catalyst loaded in a U-shaped quartz tube was first heated from room temperature to 150 °C at a rate of 10 °C min^{-1} and maintained at 150 °C for 1 h in a He gas flow (50 mL min^{-1}) to remove impurities such as water. After cooling to 50 °C, it was purged with nitrogen for 1 h to saturation, and finally, under a helium atmosphere, ramped to 800 °C at a rate of 10 °C min^{-1} for desorption. The desorbed gases were detected using a TCD.

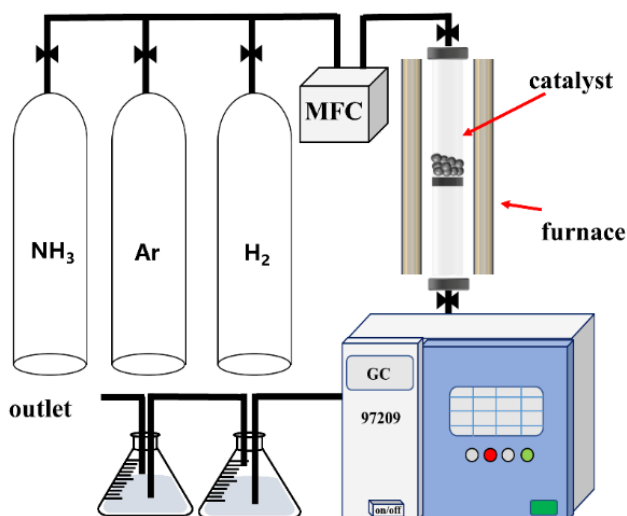**Section S2** Catalyst Activity Tests

Fig. S1. Schematic of the experimental setup used for the NH_3 decomposition test

A pure ammonia (NH_3) flow rate of 50 mL min^{-1}, corresponding to a GHSV of 15,000 mL g$_{cat}^{-1}$ h^{-1}, was maintained. Temperature-dependent NH_3 decomposition tests were conducted in the temperature range of 400 to 550 °C in 25 °C increments (60 min at

each temperature). Measurements were taken three times at each temperature point, and the average was calculated. The NH_3 conversion rate (η_{NH_3}) and H_2 formation rate (r) were calculated according to Eqs. (1) and (2):

$$\eta_{NH_3} = \frac{V_{N_2}/V_{NH_3}}{\frac{V_{N_2}}{V_{NH_3}}+0.5} \times 100\% \tag{1}$$

$$r \text{ (mmol } g_{cat}^{-1} \text{ min}^{-1}) = \frac{V_{NH_3} \cdot \eta_{NH_3} \times 1.5}{22.4 \times 0.2} \tag{2}$$

where V_{N_2} and V_{NH_3} are the molar flow rates of N_2 and NH_3 in the outlet streams, respectively.

The apparent activation energy of the catalyst was determined based on the Arrhenius equation (3) in the temperature range of 400 to 475 °C. Subsequently, a linear regression was conducted between ln r and $1000/T$, yielding a linear relationship from which the apparent activation energy was derived.

$$\ln r = \ln A - \frac{E_a}{RT} \tag{3}$$

where r represents the rate constant of the reaction, A represents the pre-exponential factor, E_a represents the activation energy, R represents the universal gas constant, and T represents the thermodynamic temperature.

Table S1. N1s XPS Analysis of Various Carbon Materials

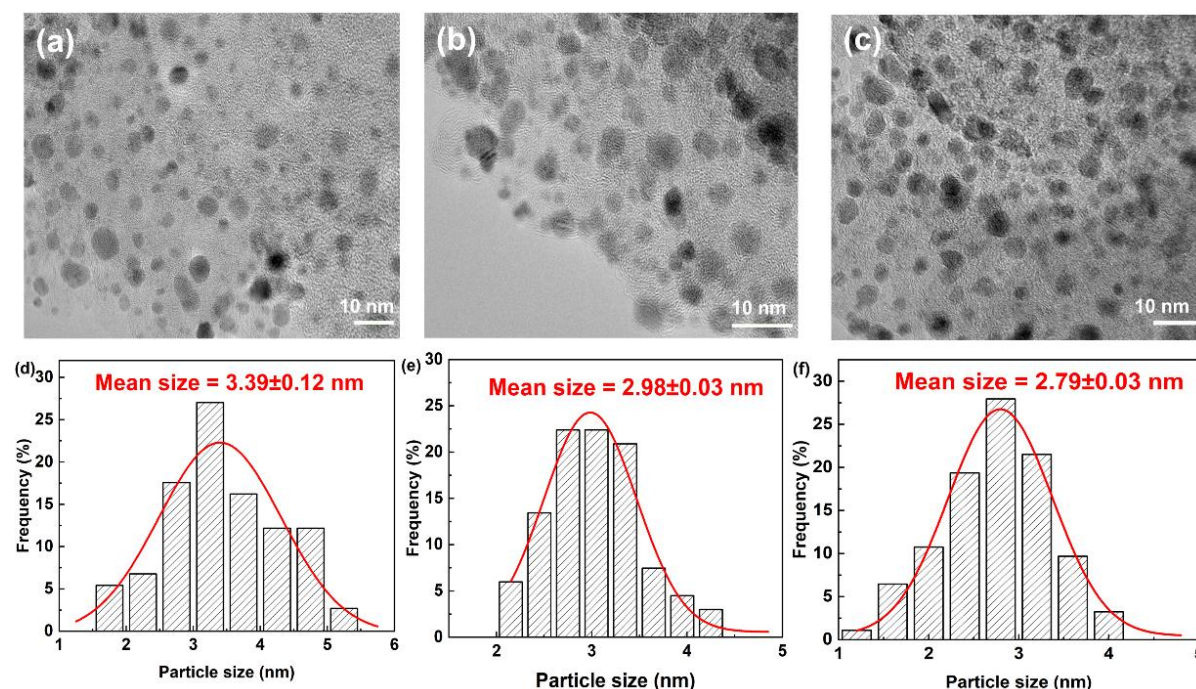| Samples	Pyridinic-N (%)	Pyrrolic-N (%)	Graphitic-N (%)	N-oxide (%)
AC-N	64.36	20.25	11.57	3.82
AC-GN	33.51	50.89	14.43	2.47

Fig. S2. TEM images and Ru particle size distribution histograms of Ru/AC (a,d), Ru/AC-N (b,e) and Ru/AC-GN (c,f)

Table S2. H_2 Formation Rate (mmol min^{-1} g$^{-1}_{cat}$) for Various Catalysts

T (°C)	Ru/AC	Ru/AC-N	Ru/AC-G	Ru/AC-GN
400	2.0	2.9	1.6	3.9
425	3.12	4.0	2.6	5.7
450	5.3	6.0	5.1	8.4
475	7.9	8.6	7.1	11.5
500	10.7	11.4	10.1	13.6
525	13.7	14.1	13.4	15.8
550	15.4	15.8	15.0	16.6

Table S3. Catalytic Activity of the Supported Ru Catalysts for NH_3 Decomposition

Catalysts	Ru content[a]	Reaction temp[b]	GHSV[c]	NH$_3$ Conv.[d]	H$_2$ formation rate[e]	Reference
Ru/AC	5.0	500	30,000	14.4	4.4	(Li *et al.* 2007)
Ru/AC	5.0	500	60,000	32.0	/	(Yin *et al.* 2004b)
Ru/AC	5.0	550	150,000	10.6	17.6	(Yin *et al.* 2004c)
Ru/AC	4.8	550	30,000	78.9	26.4	(Yin *et al.* 2004a)
Ru/CB-S	5.0	550	30,000	52.7	16.2	(Li *et al.* 2007)
Ru/CNTs	5.0	500	150,000	16.5	27.7	(Li *et al.* 2007)
Ru/CNTs	5.0	500	60,000	50.0	/	(Yin *et al.* 2004c)
Ru/CNTs	5.0	550	30,000	84.7	26.0	(Li *et al.* 2007)
Ru/CNTs-N	7.0	460	6000	92	/	(Bell *et al.* 2017)
Ru/Mgo	3.0	450	15,000	17.4	7.2	(El-kholany *et al.* 2023)

Note: [a] represents: wt%; [b]: °C; [c]: mL h^{-1} g$^{-1}_{cat}$; [d]: %; [e]: mmol min^{-1} g$_{cat}^{-1}$

References Cited

Bell, T. E., Zhan, G., Wu, K., Zeng, H. C., and Torrente-Murciano, L. (2017). "Modification of ammonia decomposition activity of ruthenium nanoparticles by N-doping of CNT Supports," *Topics in Catalysis* 60(15–16), 1251-1259. DOI: 10.1007/s11244-017-0806-0

El-kholany, M. R., Kishimoto, N., Tanaka, K., Takamura, H., and Kadota, I. (2023). "Efficient method for the preparation of ozonides under dry conditions," *Bulletin of the Chemical Society of Japan* 96(12), 1316-1318. DOI: 10.1246/bcsj.20230195

Li, L., Zhu, Z. H., Yan, Z. F., Lu, G. Q., and Rintoul, L. (2007). "Catalytic ammonia decomposition over Ru/carbon catalysts: The importance of the structure of carbon support," *Applied Catalysis A: General*, 320, 166-172. DOI: 10.1016/j.apcata.2007.01.029

Yin, S. F., Xu, B. Q., Zhu, W. X., Ng, C. F., Zhou, X. P., and Au, C. T. (2004a). "Carbon nanotubes-supported Ru catalyst for the generation of COx-free hydrogen from ammonia," *Catalysis Today*, Selections from the presentations of the 3rd Asia-Pacific Congress on Catalysis, 93–95, 27-38. DOI: 10.1016/j.cattod.2004.05.011

Yin, S.-F., Xu, B.-Q., Ng, C.-F., and Au, C.-T. (2004b). "Nano Ru/CNTs: A highly active and stable catalyst for the generation of COx-free hydrogen in ammonia decomposition," *Applied Catalysis B: Environmental* 48(4), 237-241. DOI: 10.1016/j.apcatb.2003.10.013

Yin, S.-F., Zhang, Q.-H., Xu, B.-Q., Zhu, W.-X., Ng, C.-F., and Au, C.-T. (2004c). "Investigation on the catalysis of COx-free hydrogen generation from ammonia," *Journal of Catalysis*, 224(2), 384–396. DOI: 10.1016/j.jcat.2004.03.008